Normal-incidence linear and nonlinear infrared optical response of L-valley quantum-well structures

M.J. Shaw and M. Jaros
Department of Physics, The University of Newcastle-upon-Tyne, Newcastle-upon-Tyne, United Kingdom
(Received 3 May 1994)

We present full-scale microscopic band structure calculations of the linear and nonlinear optical response of L-valley $Ga_{0.7}Al_{0.3}Sb$-AlSb and $Ga_{0.7}Al_{0.3}Sb$-$Ga_{0.4}Al_{0.6}Sb$ superlattices. We report the magnitude and spectral form of the first- and second-order optical susceptibilities. A maximum normal-incidence linear absorption coefficient of 2180 cm^{-1}, with a linewidth of 15 meV, is obtained at 10 μm. In addition, we predict that a large second-harmonic response can be induced by normally incident radiation. An account is given of the dependence of the response on the carrier concentration, and on microscopic features in the superlattice band structure. The significant enhancement of the normal-incidence response compared to other miniband absorption spectra reported in the literature is due to a combined effect of the large density of states, dispersion, and the degree of confinement.

I. INTRODUCTION

There is at present a great interest in the development of semiconductor microstructures suitable for application as infrared optical devices. In particular, systems are required which exhibit a large normal-incidence response at wavelengths of 10 to 15 μm. Recently, it has been demonstrated that such a normal-incidence response can arise from intersubband transitions involving electrons in the ellipsoidal conduction minima of suitable GaSb-AlSb and $Ga_{1-x}Al_xSb$-AlSb quantum-well structures.[1–5] For these structures, depending on the alloy composition and well width, the L-valley conduction levels can have a lower, or comparable, energy to the direct-gap minima, and can have a significant carrier population. The anisotropic effective masses of these ellipsoidal L valleys result in favorable selection rules for intersubband transitions under normal-incidence radiation. In contrast, for electrons in spherical conduction valleys, such as those in typical GaAs-$Al_{1-x}Ga_xAs$ structures, the normal-incidence transitions between conduction subbands are forbidden.[6] In addition to the relaxation of these selection rules the use of L-valley electrons can also result in an enhanced response due to the high density of states, in turn due to the large effective masses in the L valleys. These structures, therefore, appear to offer great potential as infrared detectors and other devices. The possibility of obtaining a normal-incidence response from p-type quantum-well and superlattice structures has been investigated.[7,8] Momentum mixing in the valence band can result in allowed transitions at normal-incidence between valence subbands.[9] However, the large number of closely spaced levels in the valence band makes the response of p-type structures difficult to control and very sensitive to parameters such as the doping concentration.[10,11] The n-type structures proposed here offer a more controllable response, determined by the more easily described conduction minibands.

In this paper we present microscopic calculations of the linear and nonlinear optical response in n-type $Ga_{0.7}Al_{0.3}Sb$-AlSb and $Ga_{0.7}Al_{0.3}Sb$-$Ga_{0.4}Al_{0.6}Sb$ superlattices, with quantum wells 42–55 Å wide and barriers 48–36 Å wide. The alloy $Ga_{1-x}Al_xSb$ is an indirect-gap material, with lowest conduction states of wave vector $L(\frac{1}{2},\frac{1}{2},\frac{1}{2})$, for compositions $0.2 < x < 0.5$.[12] A semi-empirical relativistic pseudopotential band structure model was employed to provide a description of the superlattices for our optical susceptibility calculations.[13] This microscopic theory enables the spectral form of the response to be predicted. Higher-lying conduction minibands are well described by this theory, allowing the evaluation of nonlinear susceptibilities in addition to the linear response. In contrast, calculations using an effective mass band structure theory are unable to describe the detailed line shapes or higher-order susceptibilities accurately. The results we obtain indicate that indeed the structures studied exhibit an enhanced linear absorption coefficient, and that this includes a significant normal incidence component. The dependence of the response on the carrier concentration is investigated and we relate the magnitude and linewidth of the response to microscopic features in the superlattice band structure. We find that the structures have optical properties favorable for device applications and that application of our theory could assist in the design of optimized structures.

II. THEORETICAL CONSIDERATIONS

The linear and second-harmonic response of the superlattices may be described by the susceptibility tensors, $\chi^{(1)}(-\omega;\omega)$ and $\chi^{(2)}(-2\omega;\omega,\omega)$, respectively. Density matrix theory was used to derive the following microscopic expressions for the susceptibilities:[14,15]

$$\chi^{(1)}_{\mu\alpha}(-\omega_\sigma;\omega_1) = -\frac{e^2N}{Vm\epsilon_0\omega_\sigma\omega_1}\delta_{\mu\alpha} + \frac{e^2}{Vm^2\epsilon_0\hbar\omega_\sigma\omega_1}\sum_k\sum_a f_a\sum_b\left[\frac{p^\mu_{ab}p^\alpha_{ba}}{(\Omega_{ba}-i\Gamma_{ba}-\omega_1)} + \frac{p^\alpha_{ab}p^\mu_{ba}}{(\Omega_{ba}+i\Gamma_{ba}+\omega_1)}\right], \quad (1)$$

and

$$\chi^{(2)}_{\mu\alpha\beta}(-2\omega;\omega,\omega) = \frac{-ie^3}{\epsilon_0 V 4\hbar m^3\omega^3}\sum_{abc}\sum_k f_0(a,k)\Big[\frac{p^\mu_{ab}p^\alpha_{bc}p^\beta_{ca} + p^\mu_{ab}p^\beta_{bc}p^\alpha_{ca}}{(\Omega_{ba}-i\Gamma_{ba}-2\omega)(\Omega_{ca}-i\Gamma_{ca}-\omega)}$$
$$+\frac{p^\alpha_{ab}p^\mu_{bc}p^\beta_{ca} + p^\beta_{ab}p^\mu_{bc}p^\alpha_{ca}}{(\Omega_{ba}+i\Gamma_{ba}+\omega)(\Omega_{ca}-i\Gamma_{ca}-\omega)} + \frac{p^\beta_{ab}p^\alpha_{bc}p^\mu_{ca} + p^\alpha_{ab}p^\beta_{bc}p^\mu_{ca}}{(\Omega_{ba}+i\Gamma_{ab}+\omega)(\Omega_{ca}+i\Gamma_{ca}+2\omega)}\Big], \quad (2)$$

where μ is the polarization of the response to applied field(s) of frequency ω and polarization α (and β). The summation $\sum_{ab(c)}$ runs over all minibands and $\sum_k$ over all wave vectors in the Brillouin zone. p^δ_{ab} represents the optical matrix element for the transition of angular frequency Ω_{ab} between minibands a and b with polarization δ. The inclusion of the damping constants Γ_{ij} provides a low-intensity approximation to the response near to system resonances. In the absence of experimental values for the transition linewidths for the particular structures considered, a value of 3 meV is used, typical for semiconductor heterostructures. Finally, $f_0(a,k)$ is the Fermi population distribution for the miniband a at wave vector k, accounting for the presence of carriers in our system. The magnitude of $\chi^{(2)}(-2\omega;\omega,\omega)$ describes the magnitude of the induced second-harmonic polarization, while $\chi^{(1)}(-\omega;\omega)$ is related to the linear absorption coefficient $\alpha_{\mu\alpha}(\omega)$ by

$$\alpha_{\mu\alpha}(\omega) = \frac{\omega}{n_0 c}\mathrm{Im}[\chi^{(1)}_{\mu\alpha}(-\omega;\omega)]. \quad (3)$$

Here, n_0 is the background refractive index, and $\chi^{(1)}$ is in SI units.

A numerical evaluation of Eqs. (1) and (2) was achieved by performing a semi-empirical relativistic pseudopotential band structure calculation,[16,17] repeated at several hundred random sampling points in the irreducible segment of the superlattice Brillouin zone. For the optical response due to transitions between conduction minibands, nonzero contributions to the susceptibilities occur only in the volume of the Brillouin zone for which the lowest conduction miniband has a significant population. Only this region of wave vector space need be sampled. Clearly the size of this region is determined by the level of doping and temperature of the superlattice. In addition, the susceptibilities are sensitive to the distribution of the carriers in the conduction minibands through the Fermi factor, $f_0(a,k)$. For calculations at 0 K, $f_0(a,k)$ assumes the values 0 or 1 depending on the miniband energy relative to the Fermi energy. For each carrier concentration considered the Fermi energy, E_F is approximately determined from the sampled band structure using the result that $\int_0^{E_F} D(\varepsilon)d\varepsilon = N_d$, where $D(\varepsilon)d\varepsilon$ is the density of states per unit volume and N_d is the carrier concentration. The effect of many-body interactions between these conduction electrons must be taken into account. For superlattice systems such as ours it is expected that of these the exchange interaction will be dominant.[18,19] An appropriate shift in the energy of occupied minibands is calculated in the manner of Bandara *et al.*,[18] and included in our calculations to account for this.

III. LINEAR RESPONSE OF $Ga_{0.7}Al_{0.3}Sb$-AlSb SUPERLATTICE

The alignment of the bulk conduction valleys and valence band edges at $Ga_{0.7}Al_{0.3}Sb$-AlSb interfaces are shown in Fig. 1. These were determined from the valence band discontinuity obtained by the method of Van de Walle.[20] The miniband structure of the $18Ga_{0.7}Al_{0.3}$-12AlSb superlattice, calculated using our pseudopotential method, is plotted along symmetry lines close to the conduction band minimum in Fig. 2. For this structure

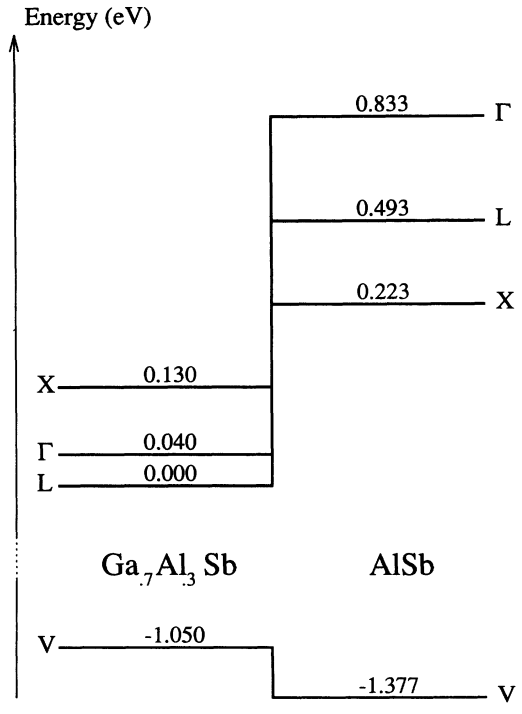

FIG. 1. A schematic diagram of the band lineups at $Ga_{0.7}Al_{0.3}Sb$-AlSb interfaces. The numerical values are calculated from Van de Walle (Ref. 20), and Casey and Panish (Ref. 12). Γ, L, and X refer to the minima at wave vectors $\frac{2\pi}{a}(0,0,0)$, $\frac{2\pi}{a}(\frac{1}{2},\frac{1}{2},\frac{1}{2})$, $\frac{2\pi}{a}(1,0,0)$, respectively, where a is the bulk lattice constant.

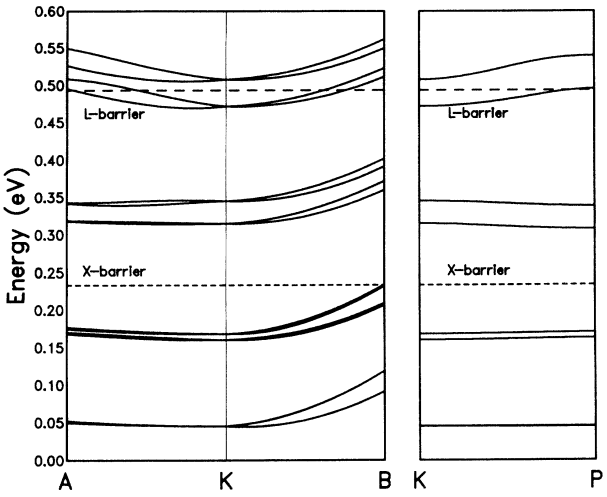

FIG. 2. The band structure of the $18Ga_{0.7}Al_{0.3}Sb$-12AlSb superlattice calculated using our semiempirical pseudopotential method. The energies are relative to the Γ conduction edge in bulk $Ga_{0.7}Al_{0.3}Sb$. A is the wave vector $\frac{2\pi}{a}(0.47, 0.47, 0)$, K is $\frac{2\pi}{a}(\frac{1}{2}, \frac{1}{2}, 0)$, B is $\frac{2\pi}{a}(0.53, 0.53, 0)$, and P is $\frac{2\pi}{a}(\frac{1}{2}, \frac{1}{2}, \frac{1}{30})$. The L and X barriers from Fig. 1 are indicated.

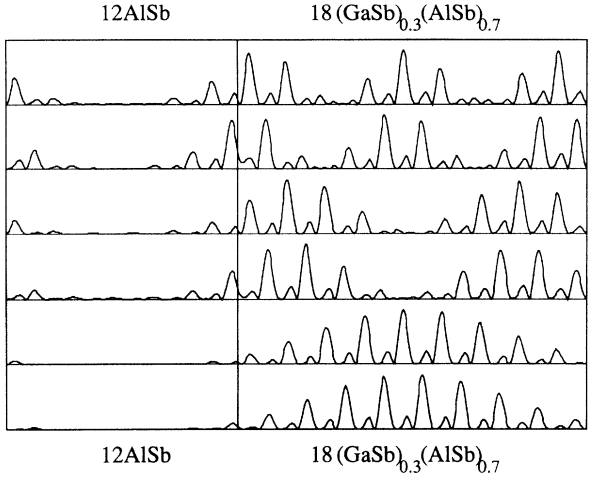

FIG. 3. The charge densities of the six lowest spin-degenerate pairs of conduction minibands at wave vector K are plotted along an axis parallel to the growth (z) axis. The charge densities have been averaged over spin-degenerate pairs.

there is very small dispersion along the growth direction z and the lowest conduction valley is centered about the line K-P (where K is the point $(\frac{1}{2}, \frac{1}{2}, 0)$ and P is the point $(\frac{1}{2}, \frac{1}{2}, \frac{1}{30})$, lying on the superlattice Brillouin zone boundary). The conduction states at this minimum result from zone folding of two equivalent bulk L valleys. Consequently, the band structure in this region consists of nearly-degenerate pairs of spin-degenerate states.[21] When the two equivalent K valleys are taken into account, there is an approximate eightfold degeneracy at the bottom of the conduction band, contributing to the very large density-of-states effective mass of the superlattice. A plot of the charge densities of the lowest conduction minibands at K is shown in Fig. 3. The charge densities are plotted along an axis in the growth direction, and the average charge density over spin-degenerate pairs is plotted. The consequence of the zone folding of two equivalent bulk L valleys is clear as, for example, the first and second spin-degenerate pairs both have ground-state envelope functions. The anisotropic nature of the L valley can clearly be seen from Fig. 4, where the energy of the lowest conduction miniband is plotted in the plane parallel to the interfaces around K, with z component of wave vector equal to zero.

The imaginary part of the components of the linear susceptibility, $\chi^{(1)}_{zz}$ and $\chi^{(1)}_{xx}$, are shown as a function of photon energy in Fig. 5, for a carrier concentration of approximately 12×10^{15} m^{-2}/well. Maximum values of 0.555 esu for $\chi^{(1)}_{zz}$ and 0.105 esu for $\chi^{(1)}_{xx}$ are obtained, in each case at a photon energy of ≈ 128 meV. These correspond [see Eq. (3)] to parallel and normal-incidence absorption coefficients of 11600 cm^{-1} and 2180 cm^{-1}, respectively. The energy at which the peaks in the linear susceptibility occur correspond very closely to the separation of the ground conduction minibands and the lower of the first-excited states at K. A secondary feature can be observed in both $\chi^{(1)}$ components at ≈ 135 meV, the energy separation of the ground and higher first-excited states at K. For each component the linewidth is ≈ 15 meV, considerably broadened from the 3-meV linewidth included in Eq. (1) by the presence of the nearly-degenerate pairs of first-excited states. The absorption peaks we observe are composed of contributions representing absorption between the occupied ground state and the various first-excited states. The normal-incidence absorption is approximately $\frac{1}{5}$ that of parallel incidence for these processes.

The maximum normal-incidence absorption coefficient of 2180 cm^{-1} is of a comparable magnitude to that reported by Samoska *et al.*[5] They observe normal-incidence absorption in a heavily doped direct-gap GaSb/AlSb superlattice resulting from interminiband transitions involving 12×10^{15} m^{-2}/well L-valley conduction electrons which have spilled over from the Γ well. While Samoska *et al.* report an absorption coefficient of 4250 cm^{-1},[22] their peak occurs at ≈ 15 μm. Since the absorption coefficient has an ω^{-1} dependence, their peak at ≈ 15 μm has effectively been enhanced by $\approx 50\%$ relative to the peak we observe at $\approx 10\mu$m. The magnitude of the normal-incidence absorption we predict is thus of the same order that Samoska *et al.* observed experimentally in a similar system. It is also pertinent to broadly compare the magnitude of our response with that of absorption due to Γ-valley carriers in $GaAs/Al_{0.5}Ga_{0.5}As$ structures reported by Levine *et al.*[23] They report an absorption coefficient of 2600 cm^{-1} for a 45° incidence at 10 μm and for a carrier concentration of 7.6×10^{15} m^{-2}/well. Our figure of 11 600 cm^{-1} for parallel incidence suggests that there is a significant enhancement due to the increased density-of-states effective mass in the L valley structure.

In Fig. 6 we compare the linear response for several different carrier concentrations (6, 9, and 12×10^{15}

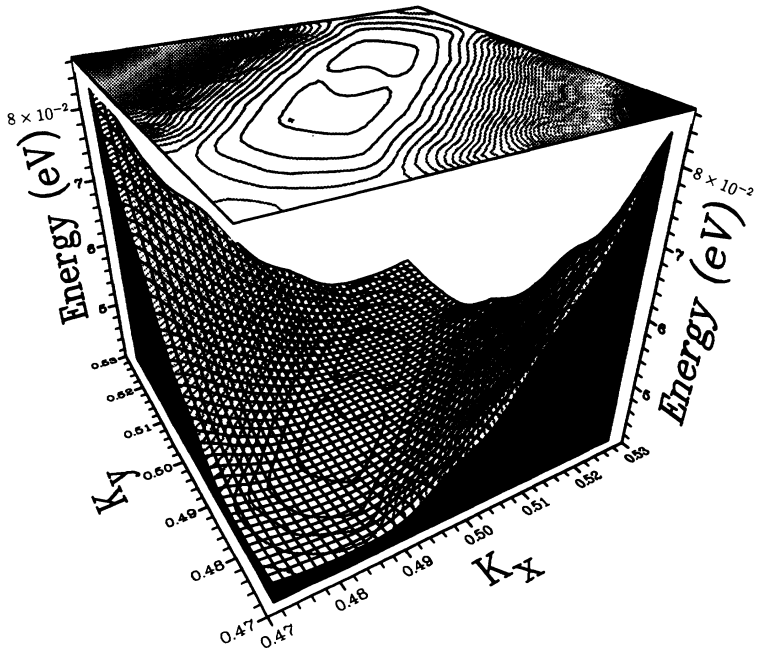

FIG. 4. The energy of the lowest conduction miniband is plotted over a plane in wave-vector space, parallel to the interfaces and with the wave vector in the growth direction equal to zero. The plane is described by $0.47\frac{2\pi}{a} \leq k_x, k_y \leq 0.53\frac{2\pi}{a}$, $k_z = 0$, where k_x, k_y, and k_z are the components of the wave vector along the x, y, and z axes.

m^{-2}/well). It can be seen from this figure that the magnitude of the response increases with the number of carriers available for absorption. The linewidth is seen to remain virtually unchanged as the doping is increased, and the line shape is qualitatively unchanged. A shift in the energy of the peak is observed—this results directly from the increase in the exchange energy as the carrier concentration is increased.

IV. LINEAR RESPONSE OF $Ga_{0.7}Al_{0.3}Sb$-$Ga_{0.4}Al_{0.6}Sb$ SUPERLATTICE

For the ease of collection in practical infrared detector devices it is preferable to have the absorbing state lie above the thermal barrier.[24] In the $18Ga_{0.7}Al_{0.3}Sb$-12AlSb superlattice, henceforth referred to as structure

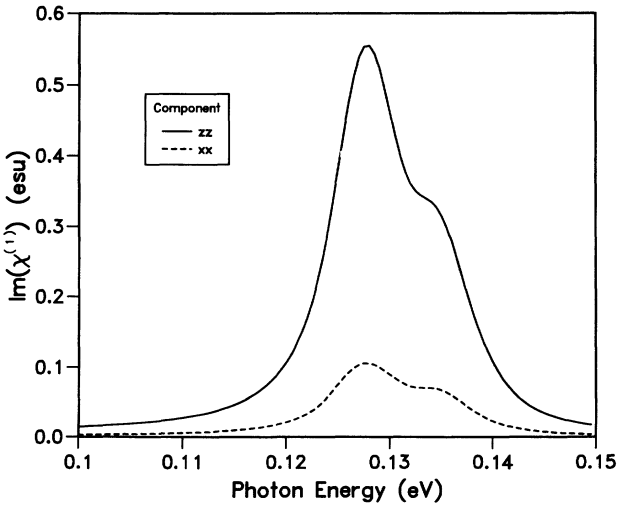

FIG. 5. The components of the imaginary part of the linear susceptibility, $\mathrm{Im}(\chi^{(1)}_{xx})$ and $\mathrm{Im}(\chi^{(1)}_{zz})$, are plotted as a function of photon energy for the $18Ga_{0.7}Al_{0.3}Sb$-12AlSb superlattice. The carrier concentration is $12\times10^{15}\mathrm{m}^{-2}$/well.

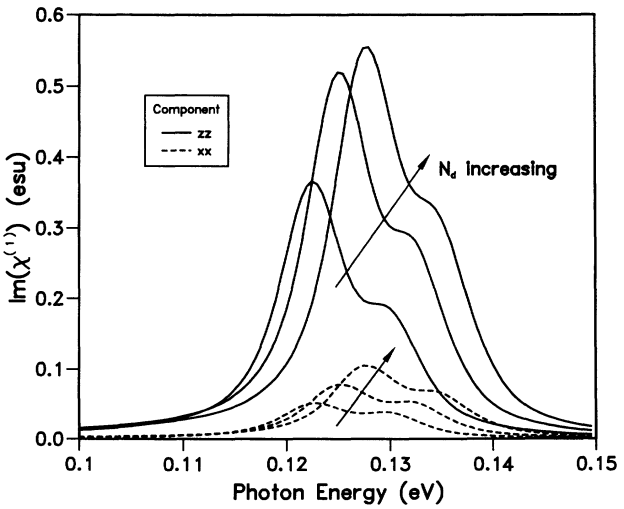

FIG. 6. The imaginary part of the linear susceptibility of $18Ga_{0.7}Al_{0.3}Sb$-12AlSb superlattice is plotted for carrier concentrations of 6, 9, and 12×10^{15} m^{-2}/well. Results are shown for both components of the linear susceptibility.

1, linear absorption at ≈ 10 μm was found to take place into the first-excited states. From Fig. 2, however, these states are seen to lie at energies well below the thermal barrier (for this structure, the X barrier). Excited carriers in this structure will be thermally bound in the well. We, therefore, consider also the response of $Ga_{0.7}Al_{0.3}Sb$-$Ga_{0.4}Al_{0.6}Sb$ superlattices, for which the alloy barriers present a lower thermal barrier. The band lineup in such structures is shown in Fig. 7. For these structures it is possible to design superlattices with first-excited states at a suitable energy for 10 μm absorption which are thermally free, yet which remain bound by the optical (L) barrier.

The band structures of the $16Ga_{0.7}Al_{0.3}Sb$-$14Ga_{0.4}Al_{0.6}Sb$ superlattice (structure 2), and the $14Ga_{0.7}Al_{0.3}Sb$-$16Ga_{0.4}Al_{0.6}Sb$ superlattice (structure 3), are shown in Figs. 8 and 9, respectively. The X and L barriers are indicated for both structures, and it can be seen that in each case the first-excited states lie close to, or above, the thermal (X) barrier. By comparison with Fig. 2 it is clear that the dispersion of the conduction minibands in the growth direction is greatly increased for the structures with alloy barriers. This is a result of the reduction in confinement, due in turn to the smaller superlattice barrier potential.

The linear response of the three structures is compared in Fig. 10, in each case for a carrier concentration of 12×10^{15} m^{-2}/well. It can be seen that the linewidth is much greater for the structures with alloy barriers (structures 2 and 3) than for the original structure, structure 1 (a linewidth of ≈ 35 meV as compared to ≈ 15 meV). These differences may be explained in terms of the different dispersions in the superlattice band structures. For the structures with alloy barriers the larger dispersion in the growth direction results in a broadening of the absorption peak, since the contributions from different wave vectors have maxima occurring over a wider range of photon energies. This spreading in energy of the contributions also results in the reduction of the maximum value obtained. The linewidth of the linear absorption peak can, therefore, be tuned by controlling the composition of the superlattice barriers. Also, we note that a significant linear absorption is predicted for structures 2

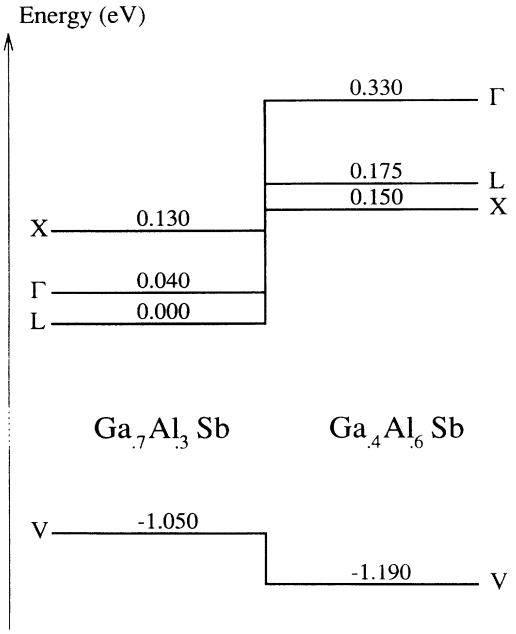

FIG. 7. A schematic diagram of the band lineups at $Ga_{0.7}Al_{0.3}Sb$-$Ga_{0.4}Al_{0.6}Sb$ interfaces. The numerical values are calculated from Van de Walle (Ref. 20), and Casey and Panish (Ref. 12). Γ, L, and X refer to the appropriate bulk minima (see Fig. 1).

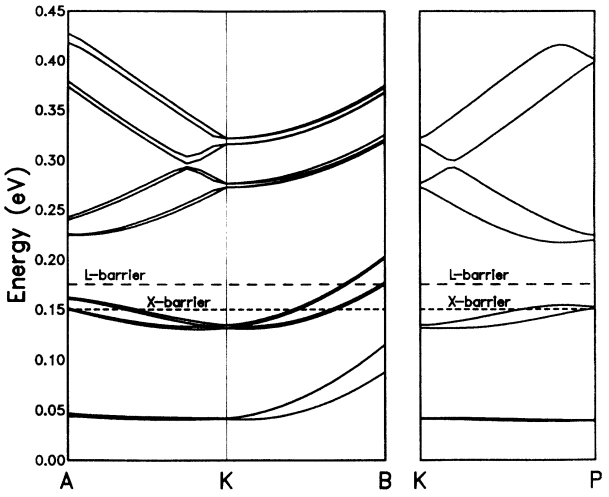

FIG. 8. The band structure of the $16Ga_{0.7}Al_{0.3}Sb$-$14Ga_{0.4}Al_{0.6}Sb$ superlattice calculated using our semiempirical pseudopotential method. The energies are relative to the Γ conduction edge in bulk $Ga_{0.7}Al_{0.3}Sb$. A, K, B, and P are as described in Fig. 2. The L and X barriers from Fig. 7 are indicated.

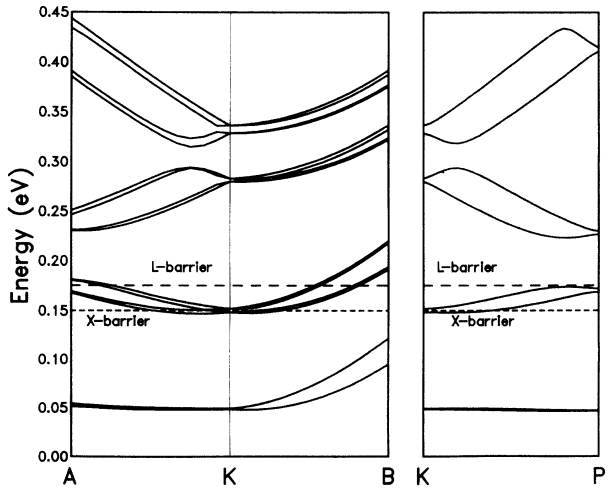

FIG. 9. The band structure of the $14Ga_{0.7}Al_{0.3}Sb$-$16Ga_{0.4}Al_{0.6}Sb$ superlattice calculated using our semiempirical pseudopotential method. The energies are relative to the Γ conduction edge in bulk $Ga_{0.7}Al_{0.3}Sb$. A, K, B, and P are as described in Fig. 2. The L and X barriers from Fig. 7 are indicated.

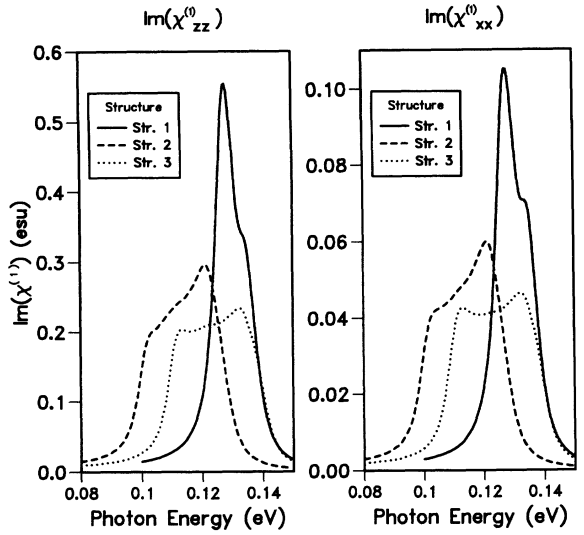

FIG. 10. The imaginary parts of the components of the linear susceptibility are plotted against photon energy for the three structures studied. Structure 1 is the $18Ga_{0.7}Al_{0.3}Sb$-$12AlSb$ superlattice, structure 2 is the $16Ga_{0.7}Al_{0.3}Sb$-$14Ga_{0.4}Al_{0.6}Sb$ superlattice, and structure 3 is the $14Ga_{0.7}Al_{0.3}Sb$-$16Ga_{0.4}Al_{0.6}Sb$ superlattice.

and 3, for which the absorption states lie close to or above the thermal barrier, convenient for practical infrared detector application.

The dependence of the response of structure 2 on carrier concentration is illustrated in Fig. 11. The frequency dependence of the linear susceptibility is shown for carrier concentrations of 6, 9, and 12×10^{15} m^{-2}/well. As in the case of structure 1 (see Fig. 6), the magnitude of the response and the energy of the peak, increase with carrier concentration. However, while the line shape in Fig. 6 remains virtually the same, in Fig. 11 the line

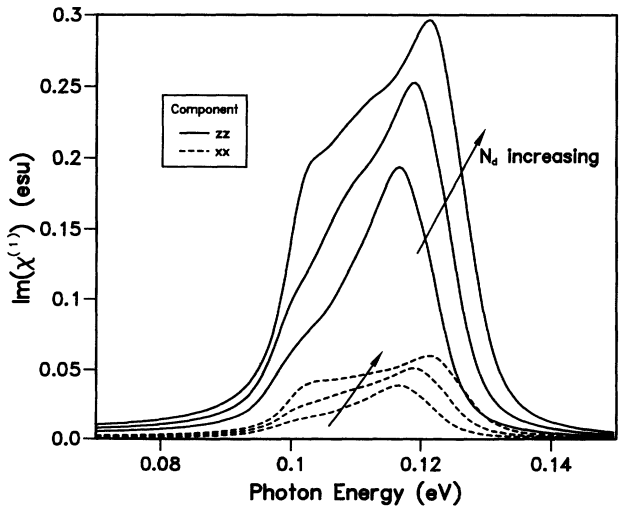

FIG. 11. The imaginary part of the linear susceptibility of $16Ga_{0.7}Al_{0.3}Sb$-$14Ga_{0.4}Al_{0.6}Sb$ superlattice is plotted for carrier concentrations of 6, 9 and 12×10^{15} m^{-2}/well. Results are shown for both components of the linear susceptibility.

shape is clearly sensitive to the number of carriers. This may again be explained by the increased dispersion in structure 2. As the number of carriers increases, contributions to $\chi^{(1)}$ occur from previously unoccupied wave vectors. For structures with large dispersion, the transition frequencies at these wave vectors may be significantly different to those of the states occupied at low carrier concentrations. Thus the line shape of the response of structures with large dispersion is more sensitive to the carrier concentration than that of structures with low dispersion. Again, we clearly see the effect that lowering the superlattice barrier potential has on the linear optical response.

V. SECOND-HARMONIC GENERATION

The microscopic theory we employ also enables the evaluation of higher-order susceptibilities. In this section we present results for the second-order susceptibility describing second-harmonic generation, $\chi^{(2)}(-2\omega;\omega,\omega)$. For the structures studied here the only two independent nonzero components of $\chi^{(2)}(-2\omega;\omega,\omega)$ are $\chi^{(2)}_{xyz}$ and $\chi^{(2)}_{zxy}$. Figure 12 shows the frequency dependence of $\chi^{(2)}_{xyz}$ and $\chi^{(2)}_{zxy}$ for the $18Ga_{0.7}Al_{0.3}Sb$-$12AlSb$ superlattice, structure 1. The response is plotted for several carrier concentrations. Both components are dominated by the contribution from the virtual processes shown schematically in Fig. 13. The presence of a third state at an appropriate energy is necessary for a large $\chi^{(2)}(-2\omega;\omega,\omega)$. From Fig. 2 it can be seen that structure 1 satisfies this condition—the separation of the first- and second-excited states is approximately equal to the

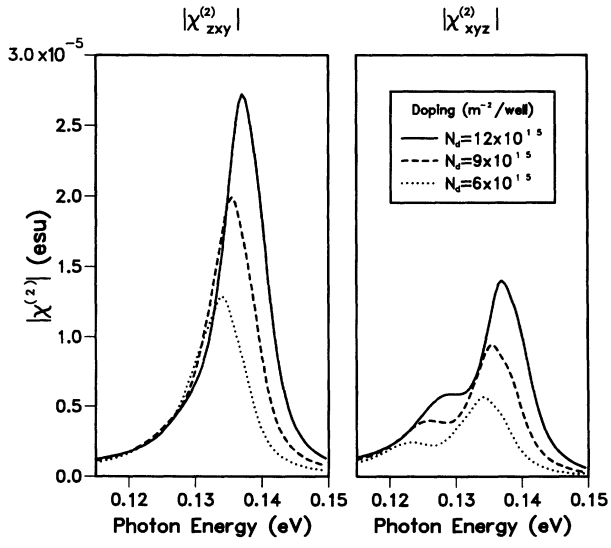

FIG. 12. The magnitude of the second-order susceptibility describing second-harmonic generation is plotted against photon energy for several carrier concentrations, for the $18Ga_{0.7}Al_{0.3}Sb$-$12AlSb$ superlattice. The components $\chi^{(2)}_{xyz}$ and $\chi^{(2)}_{zxy}$ are shown for concentrations of 6, 9, and 12×10^{15} m^{-2}/well (the notation for the susceptibilities is defined in the main text).

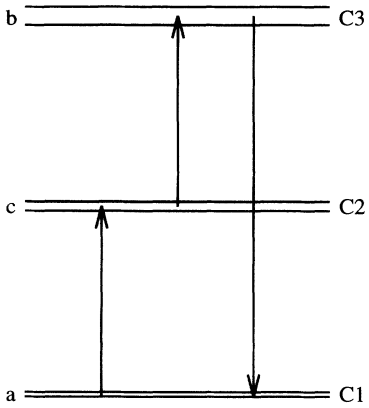

FIG. 13. A schematic diagram of the processes which dominate the second-order susceptibility in our structures. The letters a, b, and c refer to the labels in Eq. (2). States $C1$, $C2$, and $C3$ refer to the ground, first-excited, and second-excited states in the superlattice, respectively.

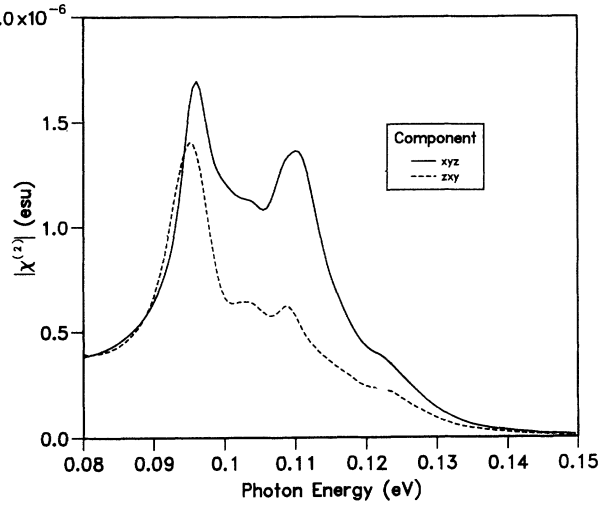

FIG. 14. The magnitude of the components of the second-order susceptibility in the $16Ga_{0.7}Al_{0.3}Sb$-$14Ga_{0.4}Al_{0.6}Sb$ superlattice are plotted against photon energy, for a carrier concentration of 12×10^{15} m^{-2}/well.

separation of the ground and first-excited states. As a result a resonant enhancement of the susceptibility occurs where the two factors in the denominator of the first term in Eq. 2 are simultaneously small. The line shape of the second-order response is determined by the detailed superlattice band structure, and the relative magnitude of the contributions from throughout the (sampled) Brillouin zone.[10] As in the case of the linear susceptibility for structure 1, the magnitude of $\chi^{(2)}(-2\omega;\omega,\omega)$ increases with carrier concentration while the line shapes remain essentially unchanged.

Finally, we compare the second-order susceptibility of structure 2. This is plotted for a carrier concentration of 12×10^{15} m^{-2}/well in Fig. 14. It can be seen that the response is an order of magnitude smaller than for structure 1. This is due to the fact that the third state in the $\chi^{(2)}$ process of Fig. 13 is no longer at the required energy for most wave vectors. The alloy barrier potential is insufficient to confine a third state, and the dispersion of the second-excited states is very large. Consequently the resonant enhancement of structure 1 is not present in structure 2. In addition to the reduced magnitude, the response of structure 2 exhibits a more complicated spectral form. This is once more a result of the increase in the dispersion arising from the reduced barrier potential.

VI. CONCLUSION

In conclusion, we have demonstrated the effectiveness of our microscopic theory in describing the magnitude and spectral form of the optical response of superlattice structures. This theory enables microscopic features of the superlattice band structure to be related to their optical response. Since the pseudopotential band structure calculations describe fully the dispersions of the minibands, including higher-lying minibands, we were able to complete a fully convergent evaluation of the line shape of the response, and to do this for the second-order susceptibility as well as the linear absorption. Our calculations may be extended to higher-order susceptibilities by straightforward application of the appropriate expressions for the susceptibilities obtained from density matrix theory.[25]

Our results indicate that n-type $Ga_{0.7}Al_{0.3}Sb$-AlSb and $Ga_{0.7}Al_{0.3}Sb$-$Ga_{0.4}Al_{0.6}Sb$ superlattices of suitable period (e.g., 91 Å) can exhibit a large optical response at infrared wavelengths due to transitions between conduction minibands involving electrons occupying L valley derived states. An enhancement to the optical response occurs due to the large density of states in these L valleys, and includes a significant normal-incidence response as a result of the anisotropic effective masses. These structures can be tuned to have a peak response at ≈ 10 μm, and it has been shown that the structures may be engineered to exhibit certain particular response characteristics. Finally, therefore, we conclude that the material system investigated shows great promise for application in practical infrared devices, and that the microscopic theory presented can play an important role in the design and optimization of such structures.

ACKNOWLEDGMENTS

We would like to thank the United Kingdom Science and Engineering Research Council and the Office of Naval Research (U.S.A.) for financial support.

[1] E. R. Brown and S. J. Eglash, Phys. Rev. B **41**, 7559 (1990).
[2] H. Xie, J. Piao, J. Katz, and W. I. Wang, J. Appl. Phys. **70**, 3152 (1991).
[3] E. R. Brown, S. J. Eglash, and K. A. McIntosh, Phys. Rev. B **46**, 7244 (1992).
[4] H. Xie, W. I. Wang, J. R. Meyer, C. A. Hoffman, and F. J. Bartoli, J. Appl. Phys. **74**, 2810 (1993).
[5] L. A. Samoska, B. Brar, and H. Kroemer, Appl. Phys. Lett. **62**, 2539 (1993).
[6] S. D. Gunapala, B. F. Levine, and N. Chand, J. Appl. Phys. **70**, 305 (1991).
[7] B. F. Levine, S. D. Gunapala, J. M. Kuo, S. S. Pei, and S. Hui, Appl. Phys. Lett. **59**, 1864 (1991).
[8] J. S. Park, R. P. G. Karunasiri, and K. L. Wang, Appl. Phys. Lett. **61**, 681 (1992).
[9] Y.-C. Chang and J. N. Schulman, Phys. Rev. B **31**, 2069 (1985).
[10] M. J. Shaw, K. B. Wong, and M. Jaros, Phys. Rev. B **48**, 2001 (1993).
[11] E. Corbin, K. B. Wong, and M. Jaros, Phys. Rev. B **50**, 2339 (1994).
[12] H. C. Casey and M. B. Panish, *Heterostructure Lasers—Part B* (Academic, New York, 1978), p. 19.
[13] M. J. Shaw and M. Jaros, Nonlinear Optics **6**, 27 (1993).
[14] P. N. Butcher and T. P. MacLean, Proc. Phys. Soc. (London) **81**, 219 (1963).
[15] C. Flytzanis, in *Quantum Electronics*, edited by H. Rabin and C. L. Tang (Academic, New York, 1975), Vol. 1A, p. 154.
[16] M. Jaros and K. B. Wong, J. Phys. C **17**, L765 (1984).
[17] M. Jaros, K. B. Wong, and M. A. Gell, Phys. Rev. B **31**, 1205 (1985).
[18] K. M. S. V. Bandara, D. D. Coon, O. Byungsung, Y. F. Lin, and M. H. Francombe, Appl. Phys. Lett. **53**, 1931 (1988).
[19] J.-W. Choe, O. Byungsung, K. M. S. V. Bandara, and D. D. Coon, Appl. Phys. Lett., **56**, 1679 (1990).
[20] C. G. Van de Walle, Phys. Rev. B, **39**, 1871 (1989).
[21] K. B. Wong, M. A. Gell, D. Ninno, and M. Jaros, Philos. Mag. Lett. **52**, L39 (1985).
[22] The figure of 8500 cm^{-1} quoted by Samoska *et al.* is an absorption coefficient per unit *well* length. For their structures this corresponds to 4250 cm^{-1} when the wells and barriers are considered.
[23] B. F. Levine, C. G. Bethea, K. K. Choi, J. Walker, and R. J. Malik, Appl. Phys. Lett. **53**, 231 (1988).
[24] B. F. Levine, C. G. Bethea, G. Hasnain, J. Walker, and R. J. Malik, Appl. Phys. Lett. **53**, 297 (1988).
[25] M. J. Shaw, D. Ninno, B. M. Adderley, and M. Jaros, Phys. Rev. B **45**, 11 031 (1992).

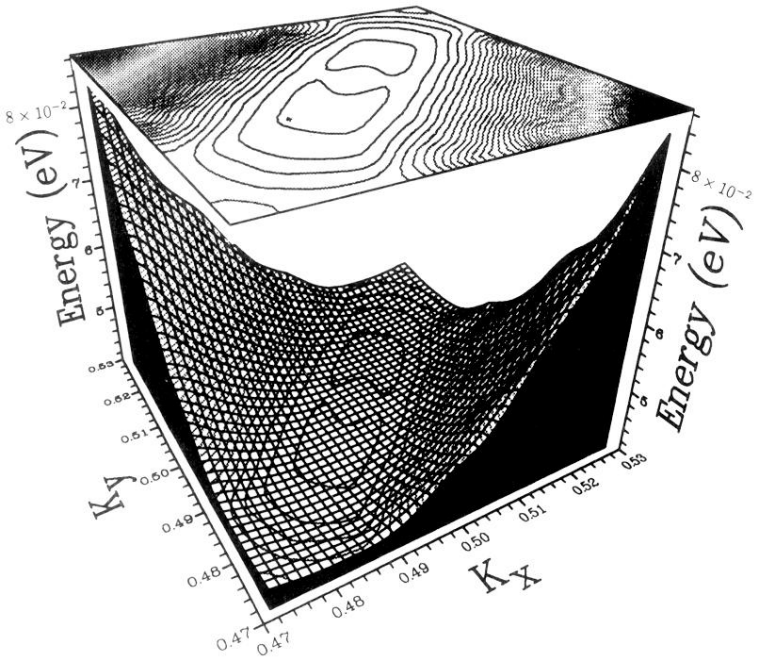

FIG. 4. The energy of the lowest conduction miniband is plotted over a plane in wave-vector space, parallel to the interfaces and with the wave vector in the growth direction equal to zero. The plane is described by $0.47\frac{2\pi}{a} \leq k_x, k_y \leq 0.53\frac{2\pi}{a}$, $k_z = 0$, where k_x, k_y, and k_z are the components of the wave vector along the x, y, and z axes.